



# Kent Academic Repository

Miao, Naihua, Xu, Bin, Bristowe, Nicholas C., Bilc, Daniel I., Verstraete, Matthieu J. and Ghosez, Philippe (2016) *First-Principles Study of the Thermoelectric Properties of SrRuO<sub>3</sub>*. *Journal of Physical Chemistry C*, 120 (17). pp. 9112-9121. ISSN 1932-7447.

## Downloaded from

<https://kar.kent.ac.uk/60248/> The University of Kent's Academic Repository KAR

## The version of record is available from

<https://doi.org/10.1021/acs.jpcc.6b02514>

## This document version

Author's Accepted Manuscript

## DOI for this version

## Licence for this version

UNSPECIFIED

## Additional information

## Versions of research works

### Versions of Record

If this version is the version of record, it is the same as the published version available on the publisher's web site. Cite as the published version.

### Author Accepted Manuscripts

If this document is identified as the Author Accepted Manuscript it is the version after peer review but before type setting, copy editing or publisher branding. Cite as Surname, Initial. (Year) 'Title of article'. To be published in *Title of Journal*, Volume and issue numbers [peer-reviewed accepted version]. Available at: DOI or URL (Accessed: date).

## Enquiries

If you have questions about this document contact [ResearchSupport@kent.ac.uk](mailto:ResearchSupport@kent.ac.uk). Please include the URL of the record in KAR. If you believe that your, or a third party's rights have been compromised through this document please see our [Take Down policy](https://www.kent.ac.uk/guides/kar-the-kent-academic-repository#policies) (available from <https://www.kent.ac.uk/guides/kar-the-kent-academic-repository#policies>).

# First-Principles Study of the Thermoelectric Properties of SrRuO<sub>3</sub>

Naihua Miao,<sup>\*,†,‡</sup> Bin Xu,<sup>¶,§</sup> Nicholas C. Bristowe,<sup>†,||</sup> Daniel I. Bilc,<sup>†,⊥</sup> Matthieu  
J. Verstraete,<sup>¶</sup> and Philippe Ghosez<sup>\*,†</sup>

*Theoretical Materials Physics, Q-MAT, CESAM, Université de Liège, B-4000 Sart Tilman, Belgium., School of Materials Science and Engineering, Beijing University of Technology, Chaoyang District, Beijing 100124, China., Physique des Matériaux et Nanostructures, Q-MAT, CESAM, Université de Liège, B-4000 Sart Tilman, Belgium., Physics Department and Institute for Nanoscience and Engineering, University of Arkansas, Fayetteville, Arkansas 72701, USA., Department of Materials, Imperial College London, Exhibition Road, London, SW7 2AZ, UK., and Molecular and Biomolecular Physics Department, National Institute for Research and Development of Isotopic and Molecular Technologies, RO-400293 Cluj-Napoca, Romania.*

E-mail: nhmiao@gmail.com; Philippe.Ghosez@ulg.ac.be

Phone: +(86) 188.012.789.59; +(32) (0)4-366.36.11. Fax: +(32) (0)4-366.36.29

---

\*To whom correspondence should be addressed

<sup>†</sup>Theoretical Materials Physics, Q-MAT, CESAM, Université de Liège, B-4000 Sart Tilman, Belgium.

<sup>‡</sup>School of Materials Science and Engineering, Beijing University of Technology, Chaoyang District, Beijing 100124, China.

<sup>¶</sup>Physique des Matériaux et Nanostructures, Q-MAT, CESAM, Université de Liège, B-4000 Sart Tilman, Belgium.

<sup>§</sup>Physics Department and Institute for Nanoscience and Engineering, University of Arkansas, Fayetteville, Arkansas 72701, USA.

<sup>||</sup>Department of Materials, Imperial College London, Exhibition Road, London, SW7 2AZ, UK.

<sup>⊥</sup>Molecular and Biomolecular Physics Department, National Institute for Research and Development of Isotopic and Molecular Technologies, RO-400293 Cluj-Napoca, Romania.

---

## Abstract

The Seebeck coefficient, thermoelectric power factor, electrical conductivity, and electronic thermal conductivity of the orthorhombic  $Pbnm$  phase of  $\text{SrRuO}_3$  are studied comprehensively by combining first-principles density functional calculations and Boltzmann transport theory. The influence of exchange-correlation functional on the Seebeck coefficient is carefully investigated. We show that the best agreement with experimental data is achieved when  $\text{SrRuO}_3$  is described as being at the limit of a half-metal. Furthermore, we analyse the role of individual symmetry-adapted atomic distortions on the Seebeck coefficient, highlighting a particularly strong sensitivity to  $R_4^+$  oxygen rotational motions, which may shed light on how to manipulate the Seebeck coefficient. We confirm that the power factor of  $\text{SrRuO}_3$  can only be slightly improved by carrier doping. Our results provide a complete understanding of the thermoelectric properties of  $\text{SrRuO}_3$  and an interesting insight on the relationship between exchange-correlation functionals, atomic motions, and thermoelectric quantities.

## Keywords

$\text{SrRuO}_3$ ; Atomic Motions; Thermoelectric Properties; Electronic Structure; First-principles Calculation

---

# 1. Introduction

SrRuO<sub>3</sub> (SRO) is a simple perovskite compound that belongs to the interesting Ruddlesden-Popper ruthenates series Sr<sub>n+1</sub>Ru<sub>n</sub>O<sub>3n+1</sub> and has been attracting researchers for a few decades due to its surprising itinerant ferromagnetism, its unusual transport properties, and the nature and degree of its electronic correlations.<sup>1</sup> Experimentally, SRO is found to adopt the ideal  $Pm\bar{3}m$  cubic perovskite structure above 950 K and then exhibits a sequence of consecutive structural and magnetic phase-transitions as the temperature is lowered. Between 825 K and 950 K it adopts a tetragonal  $I4/mcm$  structure. An orthorhombic  $Imma$  phase has been sometimes reported between 685 K and 825 K.<sup>2,3</sup> Finally, an orthorhombic  $Pbnm$  structure emerges as the ground state. The ferromagnetic transition occurs at  $\sim 160$  K.<sup>1</sup>

The  $Pbnm$  ground state of SRO is a conductive metallic oxide that is widely used as an electrode material in oxide heterostructures and superlattices,<sup>1,4,5</sup> owing to its reasonably good conducting properties<sup>6,7</sup> and its structural compatibility with other perovskite oxides. In some recent studies, SRO and related compounds were also revealed as interesting candidates for thermoelectric applications.<sup>8-12</sup> Experimentally, SRO-based solid solutions have been synthesized with different alloying elements or vacancies and their thermoelectric properties have been characterized.<sup>13</sup> Theoretically, the thermoelectric properties of SrTiO<sub>3</sub>/SrRuO<sub>3</sub> superlattices have been studied<sup>14</sup> and a metallic non-centrosymmetric ruthenate double-perovskite oxide SrCaRu<sub>2</sub>O<sub>6</sub> with large thermopower anisotropy has been proposed.<sup>15</sup> Although the electronic, structural, magnetic and lattice dynamical properties of bulk SRO have already been extensively explored theoretically,<sup>16-21</sup> to the best of our knowledge, the thermoelectric aspects has not been reported. In spite of the fact that the thermoelectric performances of SRO appear relatively modest and do not make it a very promising candidate for technological applications, it remains a very important magnetic oxide compound. Such a study will reveal interesting insight in order to provide a distinct and complementary point of view on its complex and still debated electronic properties and

---

will benefit for the development of other perovskite thermoelectric materials.

In this paper, we investigate theoretically the thermoelectric properties of bulk SRO combining first-principles density functional calculations (using various exchange-correlation functionals) and semi-classical Boltzmann transport theory. In Section 3.1, we discuss the individual influences of the exchange-correlation functional and atomic relaxations on the electronic properties and Seebeck coefficient. We emphasize that the best agreement with experimental data is obtained when SRO is described at the limit of a half-metal. We also reveal that SRO presents interesting features for spin-Seebeck applications. In Section 3.2, we investigate the influence on the Seebeck coefficient of the individual symmetry-adapted distortions giving rise to the  $Pbnm$  phase and point out the crucial role of the  $R_4^+$  oxygen rotational motions. In Sections 3.3 and 3.4, we discuss the anisotropy of the thermoelectric properties and their possible optimization with doping.

## 2. Computational methods

The structural and electronic properties have been computed within density functional theory (DFT). Most of our calculations were done using a projector-augmented wave method<sup>22</sup> as implemented in the Vienna *ab initio* Simulation Package (VASP).<sup>23</sup> The  $2s$  and  $2p$  levels of O,  $4s$ ,  $4p$  and  $5s$  levels of Sr, and  $4p$ ,  $4d$  and  $5s$  levels of Ru were treated as valence electrons. As recent theoretical and experimental works suggest that SRO is a weakly correlated compound and its physical properties can be well captured by standard DFT methods,<sup>24,25</sup> we focused at first on the usual exchange-correlation functionals: the local spin density approximation (LSDA)<sup>26</sup> and the generalized gradient approximations (GGA-PBE<sup>27</sup> and GGA-PBE<sub>sol</sub><sup>28</sup>). The cut-off energy for the plane wave basis set was set to 650 eV. The relaxation convergence for ions and electrons were  $1 \times 10^{-5}$  eV and  $1 \times 10^{-6}$  eV, respectively. A  $8 \times 8 \times 6$   $k$ -point mesh, centred in  $\Gamma$ , was used in the geometry optimization of orthorhombic SRO. For the electronic structure calculations, a denser  $16 \times 16 \times 12$   $k$ -point mesh was adopted to ensure

---

the convergence and accuracy of eigenvalues. For comparison, some additional calculations have also been performed with the CRYSTAL code<sup>29</sup> and the B1-WC hybrid functional<sup>30</sup> as previously described in Ref. 14.

The thermoelectric properties were estimated from the first-principles data using the semi-classical Boltzmann transport theory within the constant relaxation time and rigid band approximations using the BoltzTraP code.<sup>31</sup> Within the rigid band approximation, the electronic band structure is assumed to not change with carrier doping or temperature. For comparison with experiment, the total thermoelectric quantities were obtained from their averaged trace of  $xx$ ,  $yy$ , and  $zz$  components.

### 3. Results and discussion

Studying the evolution of the thermoelectric properties of SRO with temperature is *a priori* very challenging since there are various structural and magnetic phase transitions in this complicated system. However, available experiments<sup>8,9,11</sup> did not detect any drastic change of the Seebeck coefficient at these transitions: a continuous evolution was observed, suggesting a rather universal behaviour. For that reason, in our study, we will focus below on the  $Pbnm$  phase of SRO with a ferromagnetic solution in a wide temperature range. First, we will discuss the role of the exchange-correlation functionals. Then, we will investigate the effect of various lattice mode distortions.

#### 3.1 Role of the exchange-correlation functional

The total Seebeck coefficients of fully relaxed SRO, calculated using different exchange-correlation functionals, are compared in Figure 1a with available experimental data from Maekawa *et.al.* (JAC-2005),<sup>8</sup> Klein *et.al.* (PRB-2006)<sup>9</sup> and Keawprak *et.al.* (MSEB-2009).<sup>11</sup> Experimentally,  $S$  rises rapidly from 0 to 200 K before reaching a saturated value of  $\sim 30\text{-}35 \mu\text{VK}^{-1}$ . Among the calculated results,  $S$  from LSDA shows relatively large under-

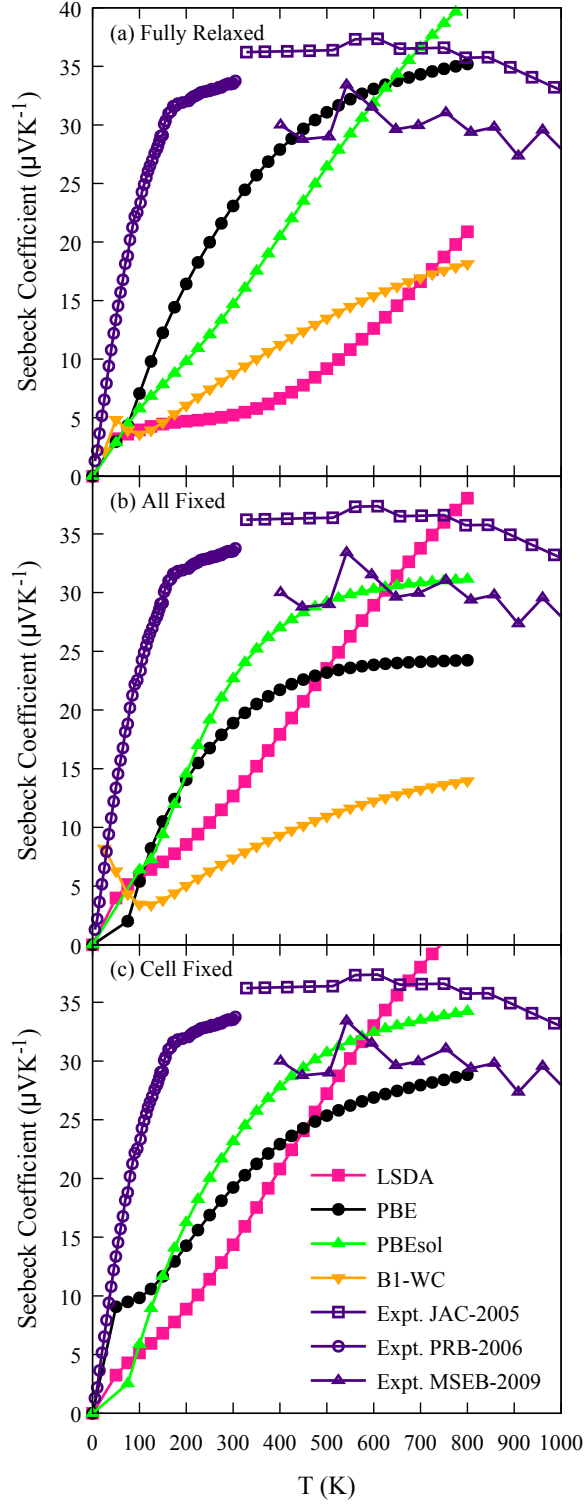


**Figure 1** The calculated Seebeck coefficient of SRO with different exchange-correlation functionals (filled symbols) compared with available experimental data (open symbols): (a) fully relaxed structure, (b) fixed experimental structure<sup>32</sup> and (c) atomic positions relaxed while keeping the lattice volume fixed to experimental data,<sup>32</sup> respectively.

---

estimation, especially at low temperatures. More significantly, the shape of the temperature evolution deviates substantially from the measured data. The magnitude of  $S$  from *PBEsol* shows a clear improvement compared with LSDA. However, some discrepancies in the temperature dependence still exist, *i.e.*, smaller slope below 200 K and no sign of saturation even above 800 K. The PBE functional yields a much better agreement with experimental data: the magnitude of  $S$  at high temperature is comparable to the experiments; the  $T$ -dependence also correctly resembles the measured trend. It is worth mentioning that, even in different experimental studies, the difference of the measured  $S$  can be as large as 20%, *e.g.*, at 450 K, the measured data are  $\sim 36 \mu\text{VK}^{-1}$  from Maekawa *et.al.*'s experiment<sup>8</sup> and  $\sim 30 \mu\text{VK}^{-1}$  from Keawprak *et.al.*,<sup>11</sup> respectively. Finally, the hybrid B1-WC functional appears significantly less accurate than the GGA: the shape is better than in LDA but the amplitudes comparable and significantly underestimate the experimental data.

In order to clarify better how the exchange-correlation functional affects the Seebeck coefficients, we recomputed  $S$  with different functionals while fixing in all calculations the lattice parameters and atomic positions to the same values, corresponding to the experimental structure<sup>32</sup> (Figure 1b). In this case,  $S$  from LSDA exhibits an improved agreement with experiment, compared with the LSDA results with the fully-relaxed structure, but the temperature dependence is still incorrect, showing a trend similar to *PBEsol* results with fully-relaxed structure. For *PBEsol*, the description of  $S$  has been greatly improved and agrees now well with experimental data.<sup>8,9,11</sup> On the other hand, the B1-WC functional does not show any improvement on the  $S$  calculated with the experimental structure. Interestingly also, using the experimental structure,  $S$  from the PBE functional above 300 K becomes smaller than for the fully relaxed structure, indicating that the deviation obtained on the crystallographic structure with different exchange-correlation functionals, influence strongly the amplitude of the computed Seebeck coefficient.

Aiming to discriminate between purely strain and internal relaxation effects, we redid the calculations while fixing the lattice constants to the experimental values but relaxing the

atomic positions. As one can see in Figure 1c, the relaxation of the atomic positions does not affect the Seebeck coefficient very much within the LSDA, but enhances its value above 400 K in both PBE and PBEsol calculations.

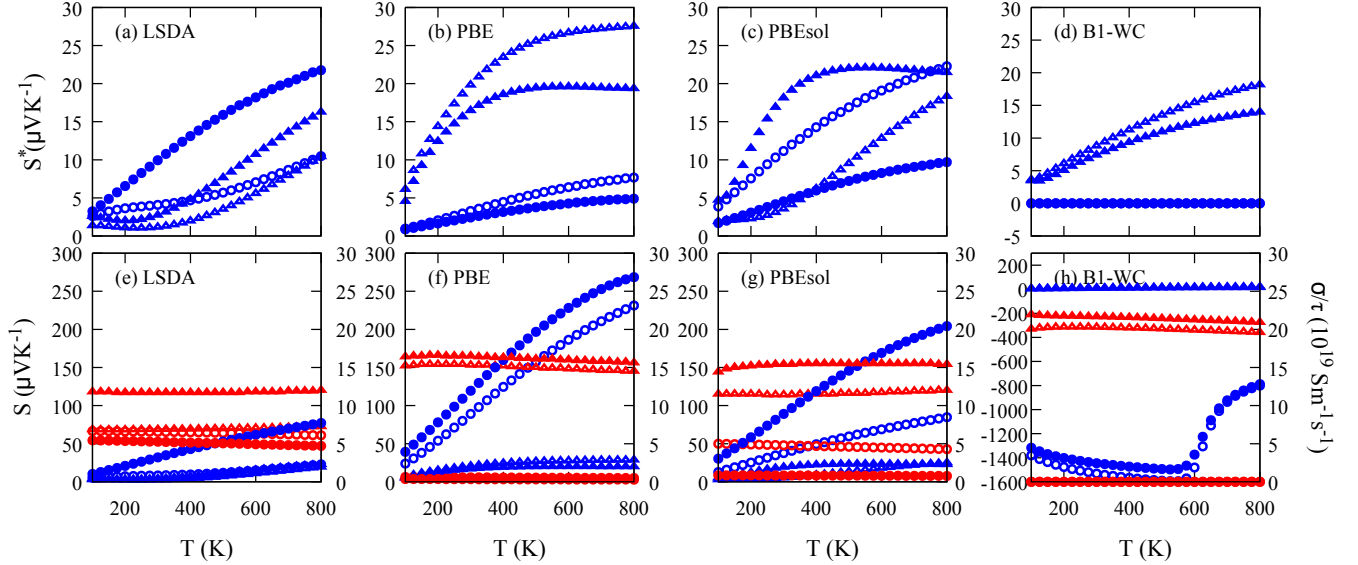


**Figure 2** Panels a, b, c, and d: Majority-spin (circles) and minority-spin (triangles) effective Seebeck coefficients ( $S^*$ ) as obtained with different functionals while using the fully relaxed (open symbols) or experimental<sup>32</sup> (filled symbols) structures. Panels e, f, g, and h: Majority-spin (circles) and minority-spin (triangles) Seebeck coefficients ( $S$ , in blue) and electrical conductivities over relaxation time ( $\sigma/\tau$ , in red) as obtained with the different functionals while using the fully relaxed (open symbols) or experimental<sup>32</sup> (filled symbols) structures.

The role of the exchange-correlation functional and crystallographic structure can be further revealed from the inspection of the spin-dependent effective Seebeck coefficient. The effective  $S^*$  can be defined as  $S_{up}^* = S_{up}\sigma_{up}/(\sigma_{up} + \sigma_{down})$  and  $S_{down}^* = S_{down}\sigma_{down}/(\sigma_{up} + \sigma_{down})$ , where majority (minority) indicates the up- (down-) spin channel, so that  $S = S_{up}^* + S_{down}^*$ . As seen from Figure 2a, within the LSDA,  $S_{up}^*$  is larger than  $S_{down}^*$  for both fully-relaxed and experimental structures. Moreover, the latter structure yields a larger effective Seebeck coefficient for both channels. For PBE, (Figure 2b), it is just the opposite:  $S$  is dominated by a large  $S_{down}^*$  and  $S_{up}^*$  is reduced. This remains true using the experimental structure, although yielding slightly smaller contributions to  $S$ . In Figure 2c, we see that, within PBEsol, the results resemble more the LDA ones using the relaxed structure while they are close

---

to those obtained within PBE by using the experimental structure. Within B1-WC, it is observed in Figure 2d that: the  $S_{up}^*$  is around 0 due to the appearance of gap in the up-spin density of states (DOS) which will be discussed later; there is not much difference on the  $S_{down}^*$ . In summary, the improved description of  $S$  achieved in PBE and in *PBEsol* while using the experimental structure is coming from a much larger and temperature-dependent  $S_{down}^*$  and a reduced  $S_{up}^*$ . The sensitive balance between up-spin and down-spin highlights that the computed  $S$  depends strongly on how each functional describes the electronic and magnetic properties. It also suggests that the down-spin electrons might have the largest Seebeck coefficient, which we will see below is not the case.

In Figure 3, we compare the spin-resolved DOS, as obtained with the different functionals using either the fully relaxed structures or the same fixed experimental structure. For the down spins (minority spin channel), the Fermi level is located in all cases more or less in the middle of an asymmetric peak, which is similar in all calculations. For the up spins (majority spin channel), the Fermi level appears always on the right side of a peak but, in this case, the position of  $E_F$  is much more sensitive to the functional and structural details. Using the LSDA and *PBEsol* at the fully-relaxed structure, the Fermi energy is inside the peak and close to its maximum. This yields a small magnetic moment on the Ru atom and a behaviour of  $S$  that poorly reproduces the experimental measurements. In the other cases, except B1-WC, the Fermi energy appears closer to the right bottom of the peak. As  $E_F$  approaches the peak bottom, the magnetic moment tends to be  $2 \mu_B$ , the value expected at the critical limit of a half-metal, and the thermoelectric properties are in much better agreement with the experiments as indicated by the calculation within *PBEsol* functional using the fixed experimental structure. Within B1-WC functional,  $E_F$  is beyond the bottom of the DOS peak and within a gap for the up-spin for both relaxed and experimental structures; this corresponds to a half-metal behaviour, which results in a poor description of Seebeck coefficient compared with experiments as discussed above, though the magnetic moment is  $2 \mu_B$ .

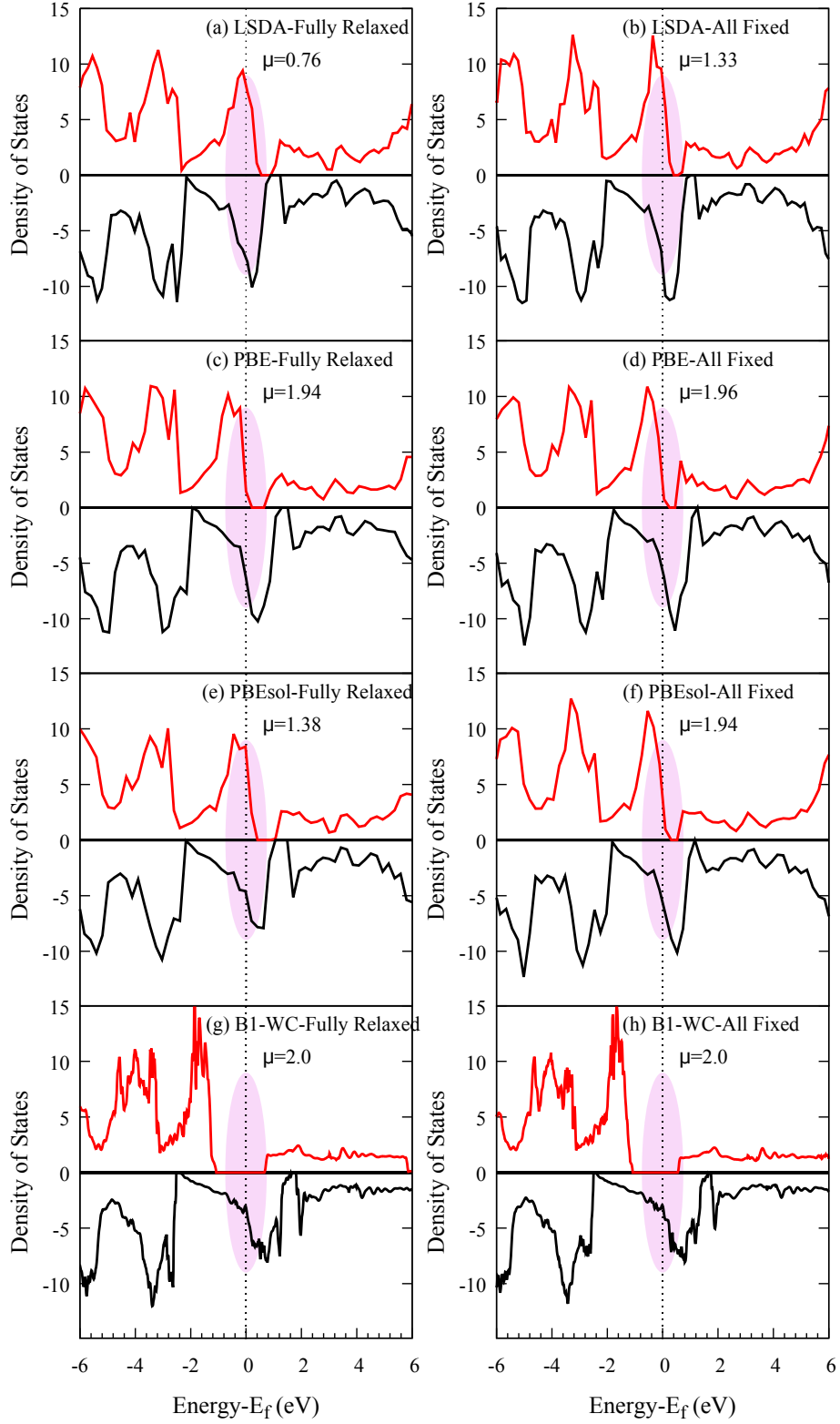


**Figure 3** The density of states (DOS, in States/eV per cell) for up-spin (red solid line) and down-spin (black solid line) channels in (a), (c), (e), and (g) pannels are calculated with fully relaxed structure; DOS in (b), (d), (f), and (h) pannels are calculated with fixed experimental structure,<sup>32</sup> respectively. The corresponding magnetic moment  $\mu$  is denoted in  $\mu_B/f.u.$

---

How can we reconcile the fact that, on one hand, the evolution of the electronic properties with the exchange functionals and atomic structures is essentially limited to the up-spin electrons and, on the other hand, the effective Seebeck coefficients show the emergence of a dominant down-spin contribution in PBE? Figure 2e-2h shows the individual Seebeck coefficients and contributions to the electrical conductivity ( $\sigma/\tau$ ) of up and down spins. In all cases, the down spins have a large conductivity and a small positive Seebeck coefficient as expected when the Fermi energy is in the middle of a peak. For the up spins, the Seebeck coefficient significantly increases and the conductivity decreases as the Fermi energy approaches the bottom of the peak. Within PBE and for the experimental structure using *PBEsol*, the up-spin electrons have clearly the largest intrinsic  $S$ . The dominant down-spin effective Seebeck coefficient is therefore not intrinsic to the down spins but emerges in fact from the drastic reduction of the up-spin electrical conductivity. In the case of B1-WC, there is a large negative up-spin Seebeck coefficient, attributed to the gap in the up-spin DOS as shown in Figure 3h.

There has been a long debate about the possible half-metal nature of  $\text{SrRuO}_3$ .<sup>20,21,24</sup> As regards the thermoelectric properties, our study reveals that the experimental behaviour is much better reproduced when the magnetic moment tends toward  $2.0 \mu_B$  and the compound likely approaches the limit of a half-metal, but is not exactly a half-metal.

We further notice that the Seebeck coefficient is significantly different for up and down spins, suggesting that  $\text{SrRuO}_3$  might be an interesting candidate for spin-Seebeck applications.

## 3.2 Role of lattice mode distortions

The orthorhombic  $Pbnm$  phase of SRO appears as a small distortion of the ideal  $Pm\bar{3}m$  cubic perovskite structure, mainly arising from the combination of rotations and tilts of the oxygen octohedra (corresponding to  $a^-a^-b^+$  in Glazer's notations<sup>35</sup>). As previously discussed for instance in Ref. 21, the distortion mainly arises from the combination of in-phase rotations

**Table 1** Symmetry-adapted modes analysis (with the corresponding irreducible representations) for the ground state SrRuO<sub>3</sub> after different relaxations (full relaxation, or only allowing volume/atomic optimization) within LSDA, PBE, PBE*sol* and B1-WC exchange-correlation functionals (Exc.). L.P. and A.P. denote the lattice parameters and atomic positions, respectively. Theo. refers to theoretically optimized structural data, and Expt. indicates the results calculated with experimental structure from Ref. 32, respectively. Amplitudes in Å for various modes have been obtained with Amplitode.<sup>33,34</sup> The corresponding magnetic moment is also given in  $\mu_B$ /f.u. These atomic motions are also illustrated in Figure 4.

Exc.	L. P.	A. P.	Oxygen		Rotation		Anti-polar Motion		Jahn-Teller	$\mu$	$V$ (Å <sup>3</sup> )
			R <sub>4</sub> <sup>+</sup>	M <sub>3</sub> <sup>+</sup>	X <sub>5</sub> <sup>+</sup>	R <sub>5</sub> <sup>+</sup>	M <sub>2</sub> <sup>+</sup>				
LDA	Theo.	Theo.	0.9878	0.6569	0.2798	0.0481	0.0024	0.76	231.23		
	Expt.	Expt.	0.8395	0.5631	0.1753	0.0348	0.0131	1.33	241.52		
	Expt.	Theo.	0.9331	0.6317	0.2821	0.0494	0.0023	1.21	241.52		
PBE	Theo.	Theo.	1.0257	0.7523	0.3209	0.0488	0.0046	1.94	233.28		
	Expt.	Expt.	0.8395	0.5631	0.1753	0.0348	0.0131	1.96	241.52		
	Expt.	Theo.	0.9530	0.7402	0.3187	0.0484	0.0021	1.98	241.52		
PBE <i>sol</i>	Theo.	Theo.	1.0361	0.7490	0.3196	0.0487	0.0072	1.38	222.74		
	Expt.	Expt.	0.8395	0.5631	0.1753	0.0348	0.0131	1.90	241.52		
	Expt.	Theo.	0.9530	0.7402	0.3187	0.0484	0.0021	1.94	241.52		
B1-WC	Theo.	Theo.	0.9711	0.7399	0.3126	0.0414	0.0078	2.00	241.35		
	Expt.	Expt.	0.8395	0.5631	0.1753	0.0348	0.0131	2.00	241.52		
	Expt.	Theo.	-	-	-	-	-	-	-		

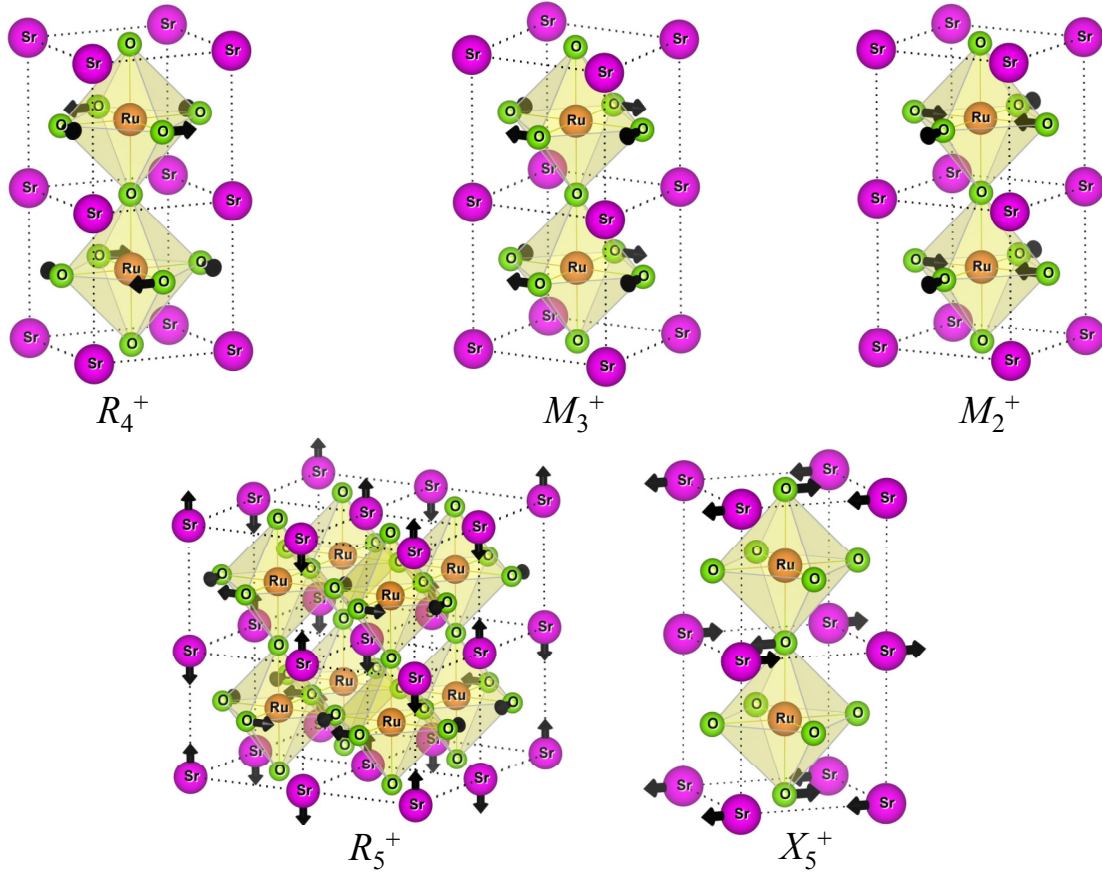


**Figure 4** A schematic illustration of relevant phonon modes of  $\text{SrRuO}_3$  with corresponding atomic motions in crystal lattice.  $R_4^+$ ,  $M_3^+$ , and  $M_2^+$ , on the first line, are pure oxygen motions, and  $X_5^+$  and  $R_5^+$  below are cationic motions, respectively. The black arrows indicate atomic motions.

---

of the oxygen octahedra ( $M_3^+$  symmetry) along  $z$  and anti-phase rotations of the oxygen octahedra along  $x$  and  $y$  ( $R_4^+$ ) but also involves anti-polar cationic motions ( $X_5^+$  and  $R_5^+$ ) and even a small Jahn-Teller type distortion ( $M_2^+$ ), allowed in the  $Pbnm$  symmetry.<sup>36,37</sup> All these relevant atomic motions are illustrated in Figure 4. In order to understand how the thermoelectric properties evolve not only with the functional but also along the sequence of phase transitions from  $Pm\bar{3}m$  to  $Pbnm$ , it is interesting to investigate how these individual motions eventually affect the Seebeck coefficient.

The structure-related information from symmetry-adapted mode analysis, calculated magnetic moment and lattice volume of various constrained structures are summarized in Table 1 and Table S1 (Supporting Information). Compared with experimental data, it shows that the DFT simulations typically overestimate the oxygen rotations and anti-polar motions, but underestimate the Jahn-Teller distortion, volume and magnetic moment except for the case of PBE. Among these modes, the largest relative discrepancy between fully relaxed structures and the experimental ones is for the weak  $M_2^+$  distortion. In the case of LSDA and PBEsol, together with Figure 1a, 1b, and 1c, it can be observed that the volume and magnetic states affect the Seebeck coefficient, but the role of atomic motions is complex.

To identify the role of individual atomic motions, Figure 5 plots the calculated  $S$  with the PBE functional using structures with various mode configurations, different magnitude of Jahn-Teller distortions and finite-temperature experimental structures.<sup>38</sup> Among all the mode configurations, the oxygen rotations appears to play the central role: the  $R_4^+$  oxygen rotations enhance the value of  $S$  significantly, while the appearance of  $M_3^+$  tends to reduce it. As evidenced in Figure S1 (Supporting Information), the origin of that can be traced back in the up-spin DOS which changes strongly when tuning the  $R_4^+$  mode amplitude. This suggests possible strategies to optimize the  $S$  by applying tensile epitaxial strain, or decreasing the tolerance factor by chemical engineering, *e.g.*, Sr  $\rightarrow$  Ca  $\rightarrow$  Mg. Also, as the  $R_4^+$  mode appears in all the intermediate phases of SRO<sup>21</sup> (from 0 to  $\sim 950$  K) and contributes greatly to the total  $S$  of SRO, this explains why the experimentally measured  $S$  are almost constant even

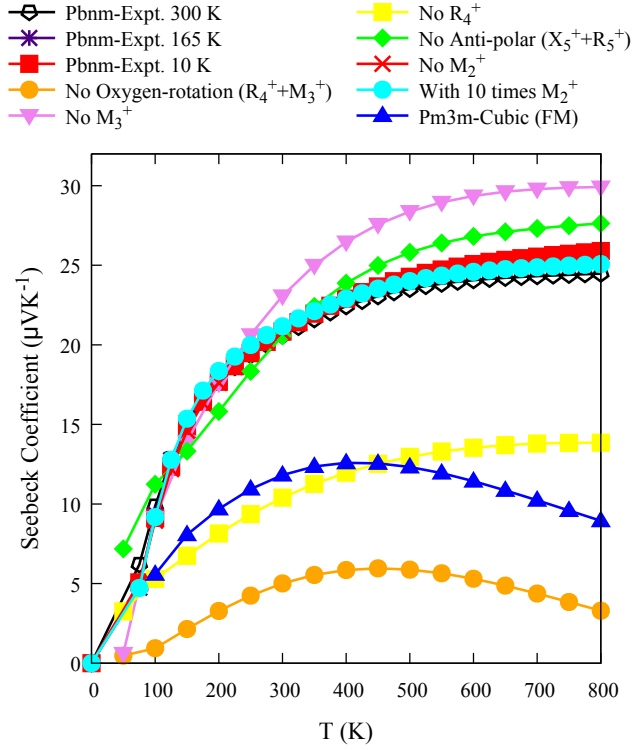


**Figure 5** The Seebeck coefficient of SRO (filled symbols) calculated using PBE functional with various mode configurations and in the experimental structures at different temperatures<sup>38</sup> in comparison to experimental data (open symbols). Note that the calculated  $S$  for *Pbnm*-Expt.300 K and *Pbnm*-Expt.165 K structures are very close.

---

in the phase-transition regions. Similar to  $M_3^+$ , the anti-polar motions slightly lower the  $S$  as shown in Figure 5. As neither the Jahn-Teller-like distortion nor the temperature-dependent crystal structures could change the calculated magnetic moment and DOS obviously, no notable difference is observed for the Seebeck coefficient where the effect is almost negligible compared with that from volume, magnetic states and  $R_4^+$  mode.

Note that the calculated  $S$  of cubic phase is much smaller than the experimental values which may be due to the limitation of FM solution used herein. As discussed above and shown in Figure 1a, the PBE functional produces the most reasonable values and trend of Seebeck coefficient for the fully relaxed structures compared with the one using experimental structures. Hence, we will report the results from PBE calculations in the following text, unless stated otherwise.

### 3.3 Anisotropy of Seebeck coefficient, electrical and thermal conductivity

In Figure 6, we plot the calculated Seebeck coefficient along different directions and compare with available experimental data, where the total Seebeck coefficient  $S_{total}$  is an average of the  $S_{xx}$ ,  $S_{yy}$  and  $S_{zz}$ . It seems that, below 450 K, the Seebeck coefficient is not as anisotropic as that above 450 K. The value of  $S_{xx}$  is always slightly larger than  $S_{yy}$  and  $S_{zz}$  and becomes closer to  $S_{yy}$  above 450 K. Unlike  $S_{zz}$  which becomes saturated above 450 K,  $S_{xx}$  and  $S_{yy}$  keep increasing in the entire temperature range, showing a similar behaviour. This is consistent with the  $Pbnm$  crystal structure, since the  $a$  and  $b$  lattice parameters are almost identical. However, compared with the experiments, it seems that the  $S_{zz}$  is closer to the experimental data and trend in Keawprak *et.al.*'s work,<sup>11</sup> suggesting that their samples had a preferential orientation.

Figure 7 shows the calculated electrical conductivity divided by relaxation time ( $\sigma/\tau$ ), compared with the experimental electrical conductivity  $\sigma$ . It should be noted that the electrical conductivity of the single crystal and polycrystal are quite different in various

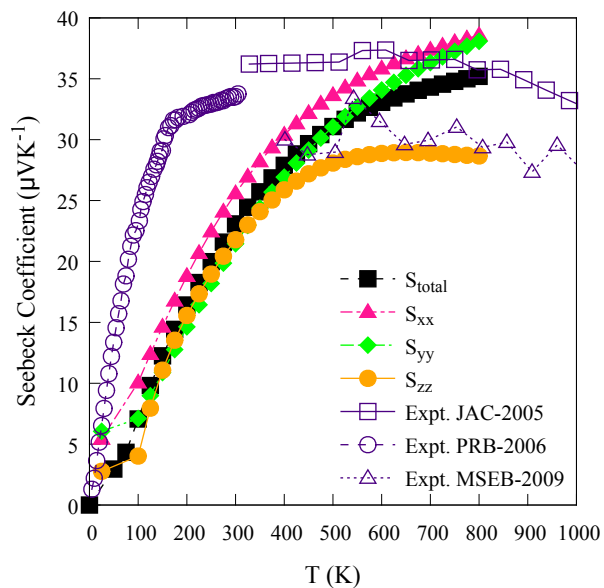


**Figure 6** The calculated direction-dependent Seebeck coefficient of SRO (filled symbols) compared with experimental data<sup>8,9,11</sup> (open symbols).

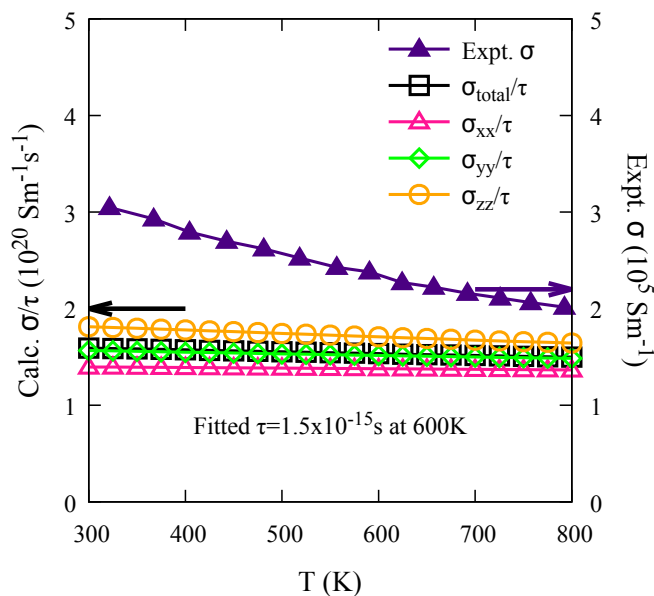


**Figure 7** The calculated direction-dependent  $\sigma/\tau$  of SRO (open symbols, left y-axis) as a function of temperature compared to experimental electrical conductivity<sup>10</sup> (filled symbols, right y-axis).

experiments.<sup>10,11</sup> We compared our result with the experimental data measured on the single crystal<sup>10</sup> herein. The total  $\sigma/\tau$  has a much weaker temperature dependence compared with the experimental  $\sigma$ , indicating that the relaxation time  $\tau$  is decreasing slightly with the increase of temperature. If we fit the calculated total  $\sigma/\tau$  (obtained by an average of the xx, yy and zz components of  $\sigma/\tau$ ) with the experimental value of  $\sigma$ , the obtained relaxation time at 600 K is  $1.5 \times 10^{-15}$  s, which is a typical value for the scattering time in oxides. As illustrated in Figure 7, obviously, the  $\sigma/\tau$  is anisotropic, where the largest difference can be up to 35% between the xx and zz components. Unfortunately, there is no experimental measurement or theoretical literature on the electrical conductivity along different directions available for comparison. Our calculations can provide a reference for future works.

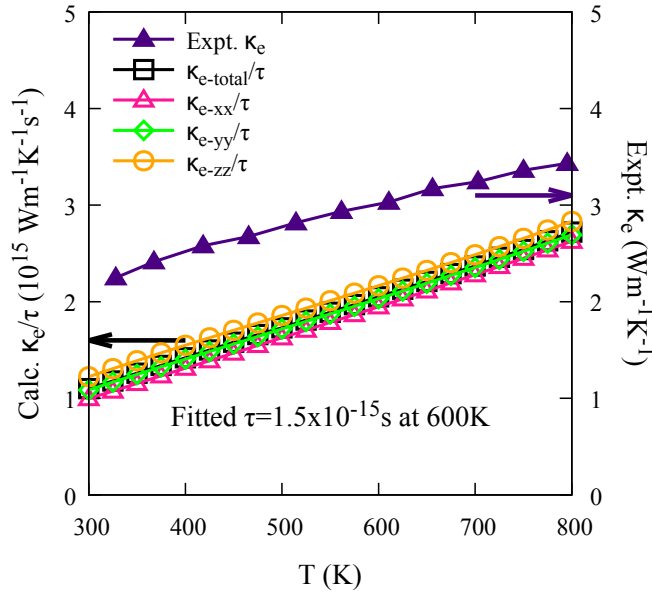


**Figure 8** The calculated direction-dependent  $\kappa_e/\tau$  of SRO (open symbols, left y-axis) as a function of temperature compared to experimental electronic thermal conductivity<sup>8</sup> (filled symbols, right y-axis).

As seen from Figure 8, contrary to the  $\sigma/\tau$ , the electronic thermal conductivity divided by relaxation time ( $\kappa_e/\tau$ ) is increasing with the increase of temperature and it looks relatively isotropic, *e.g.*, the calculated value of  $\kappa_e/\tau$  along different directions are quite close to each other. The xx and yy components of  $\kappa_e/\tau$  are extremely close and both of them are a little bit smaller than that along the zz component. Compared with the experimental

---

thermal conductivity,<sup>8</sup> the calculated total  $\kappa_e/\tau$  also increases with the increase of temperature but in relatively smaller amplitude, suggesting that the value of  $\tau$  is decreasing when temperature increases which is in agreement with the trend of  $\tau$  indicated by the electrical conductivity discussed above. If we fit the calculated total  $\kappa_e/\tau$  to experimental  $\kappa_e$ , the obtained relaxation time is  $\sim 1.5 \times 10^{-15}$  s at 600 K, which is in good agreement with the fitted value from the calculated  $\sigma/\tau$  against experimental electrical conductivity as mentioned above. Interestingly, it seems that the value of relaxation time  $\tau$  is decreasing from  $\sim 2 \times 10^{-15}$  s to  $\sim 1.2 \times 10^{-15}$  s with the increase of temperature from 300 K to 800 K. As the relaxation time of SRO only varies slightly with temperature, we will adopt the  $\tau$  value of 2 fs for 300 K, 1.75 fs for 450 K and 1.5 fs for 600 K to calculate the thermoelectric quantities in the following text, respectively.

### 3.4 Optimal thermoelectric quantities

The calculated direction-dependent Seebeck coefficient, electrical conductivity, electronic thermal conductivity, and power factor at 300 K, 450 K and 600 K as a function of chemical potential from -0.5 eV to 0.5 eV are given in Figure 9. As observed from Figure 9a, the Seebeck coefficient varies significantly with chemical potential and the trend of  $S_{zz}$  is quite different from that of  $S_{xx}$  and  $S_{yy}$ . At 600 K, the maximum Seebeck coefficient of  $\sim 52 \mu\text{VK}^{-1}$  (the yy component) can be reached at a chemical potential of around 0.07 eV. Figure 9b shows that the electrical conductivity decreases with chemical potential from -0.5 eV to 0.5 eV, where strong peak is observed for the  $\sigma_{zz}$ . A similar trend can be observed for the electronic thermal conductivity as shown in Figure 9c, which indicates that the relationship between the electrical conductivity and electronic thermal conductivity in SRO fits the so called Wiedemann-Franz law ( $\kappa_e = L\sigma T$ ) for conductors, where  $L$  is the Lorenz number. It seems that the zz component of  $\sigma$  and  $\kappa_e$  is always larger than that of the other components at a given temperature. Finally, we plot the power factor in Figure 9d. The optimum PF (zz component) for the undoped crystal at 300 K is around  $4 \times 10^{-4} \text{ Wm}^{-1}\text{K}^{-2}$ , which is close to

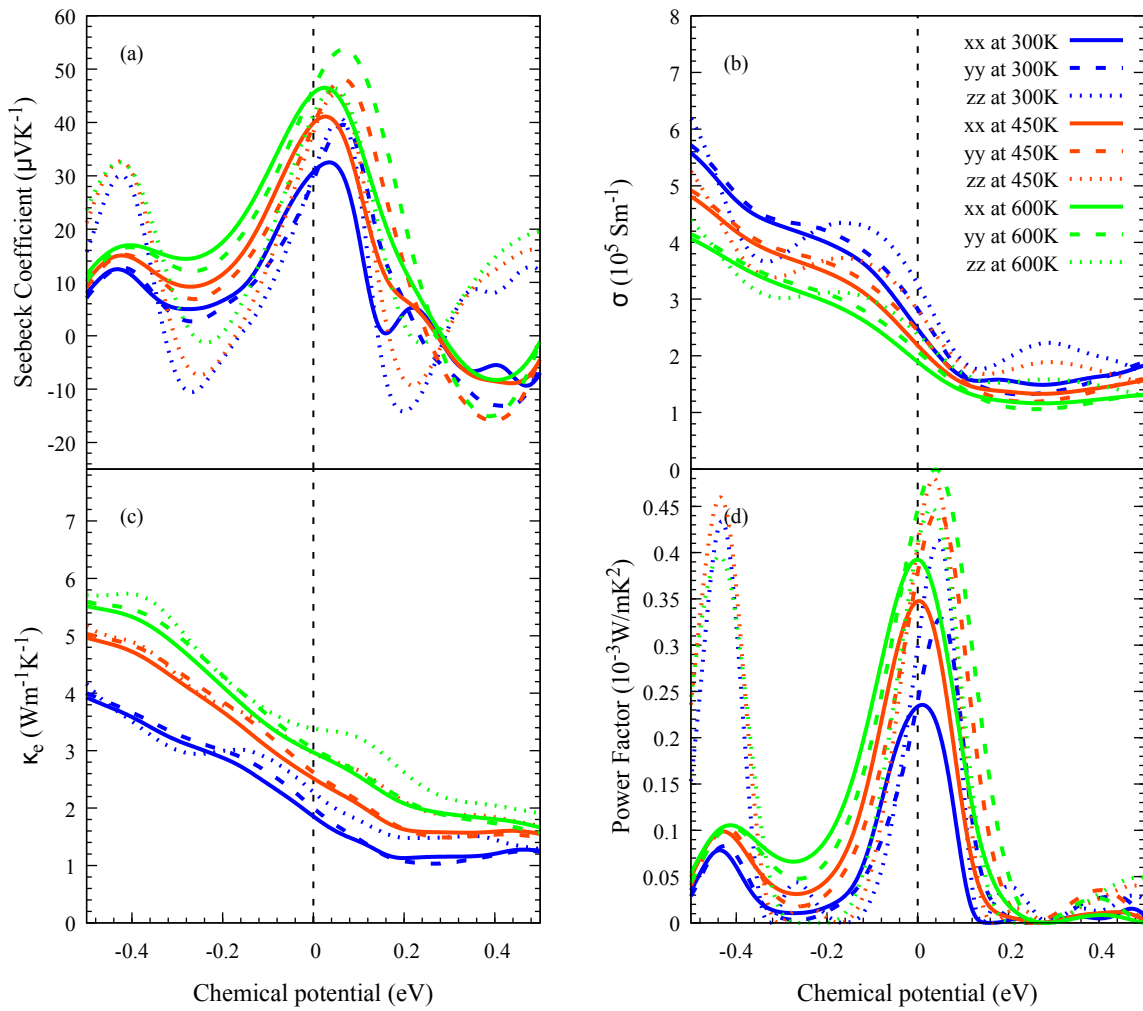


**Figure 9** The calculated Seebeck coefficient (a), electrical conductivity (b), electronic thermal conductivity (c), and power factor (d) of SRO as a function of chemical potential.

the previous experimental measurement.<sup>8</sup> At 450 K, a larger value of  $\sim 5 \times 10^{-4} \text{ Wm}^{-1}\text{K}^{-2}$  can be obtained for the zz component by n-type doping at the chemical potential of 0.05 eV where a maximum value of PF for the yy component can also be reached at 600 K. As seen from the figure, a comparable PF of  $\sim 4.7 \times 10^{-4} \text{ Wm}^{-1}\text{K}^{-2}$  for the zz component can be achieved at -0.4 eV, namely by p-type doping, but this might be hard to reach experimentally.

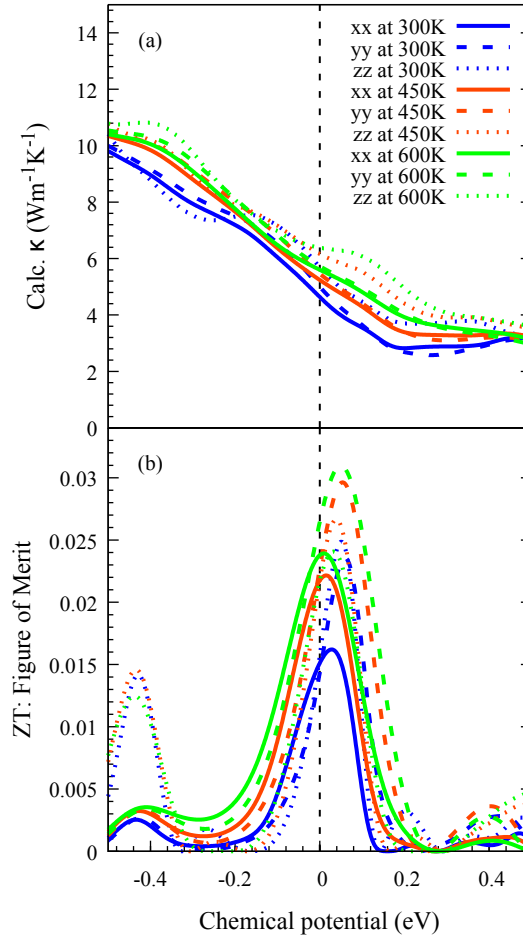


**Figure 10** The calculated (a) thermal conductivity and (b) figure of merit of SRO as a function of chemical potential.

Experimentally, the electronic contribution to total thermal conductivity in SRO is around 40% at 300 K, 48% at 450 K and 53% at 600 K, respectively.<sup>10</sup> Using these proportions for  $\kappa_e/\kappa$ , we plotted the total thermal conductivity and figure of merit ( $ZT$ ) in

---

Figure 10. From Figure 10a, it is observed that the thermal conductivity increases slightly with temperature and decreases with chemical potential from -0.5 eV to 0.2 eV and then becomes flat. The maximum value is always achieved for the  $zz$  component. As shown in Figure 10b, the optimal  $ZT$  are  $\sim 0.029$  at 450 K and 0.032 at 600 K (the  $yy$  component) within the shown chemical potential range, respectively, which is close to the previous experimental data.<sup>8,11</sup> According to Figure 10b, unfortunately, the  $ZT$  of SRO could not be improved dramatically by carrier doping. As its thermal conductivity is relatively large, *i.e.*, the  $\kappa_{min}$  is around  $2 \text{ Wm}^{-1}\text{K}^{-1}$ , which is a few times larger than that of so called low- $\kappa$  compounds,<sup>39</sup> future work would be encouraged to focus on the reduction of the  $\kappa$ .

## 4. Conclusions

We have comprehensively investigated the thermoelectric properties of SRO using first-principles density functional calculations and Boltzmann transport theory. Among the LSDA, PBE,  $PBE_{sol}$  and B1-WC exchange-correlation functionals, PBE is the most suitable one to describe the thermoelectric quantities of SRO and a reasonable agreement with experiments has been achieved. LSDA and B1-WC fail to describe the system reasonably. In the case of  $PBE_{sol}$ , the trend of  $S$  can be captured correctly only with the fixed experimental structure thanks to the resulting improvement of DOS around Fermi level. According to our investigations, the thermoelectric properties are very sensitive to the electronic properties: they are better described when the magnetic moment tends toward  $2 \mu_B$  and SRO approaches the limit of a half-metal. Moreover, they are also affected by the volume and atomic motions, especially the  $R_4^+$  mode of oxygen rotations. The appearance of  $R_4^+$  mode in all the intermediate phases of SRO contributes greatly to the value of  $S$  and benefit to the enhancement of  $S$ , while the anti-polar motions and the  $M_3^+$  mode of oxygen rotations reduce  $S$  and contribute less than the former. Hence, it might be beneficial to have  $R_4^+$  oxygen motions included when designing the ruthenate related thermoelectric materials. We

---

may maximize the  $R_4^+$  mode by, for example, epitaxial strain, or decreasing the tolerance factor, *e.g.*, Sr  $\rightarrow$  Ca  $\rightarrow$  Mg. Using the fitted scattering relaxation time, we obtain the optimal  $ZT$  of  $\sim 0.029$  at 450 K and  $\sim 0.032$  at 600 K (the  $yy$  component), respectively, which is in good agreement with previous experimental result. Unfortunately, since neither the power factor nor the figure of merit can be greatly improved by carrier doping, more future work on reducing the thermal conductivity are encouraged to achieve a better thermoelectric performance of SRO.

## Acknowledgement

This work is supported by the ARC project TheMoTherm (Grant No. 10/15-03) and the F.R.S.-FNRS PDR project HiT4FiT. P.G. thanks the Francqui Foundation for a Research Professorship. N.C.B thanks the Royal Commission for the Exhibition of 1851 and Imperial College London for a Junior Research Fellowship and support from the Thomas Young Centre under grant TYC-101. D.I.B. thanks the Romanian National Authority for Scientific Research, CNCS-UEFISCDI (Grant No. PN-II-RU-TE-2011-3-0085). The CECI (<http://www.ceci-hpc.be>, F.R.S.-FNRS Grant 2.5020.11), PRACE-2IP on Huygens and Hector (EU FP7 Grant RI-283493), CISM-UCLouvain, and SEGI-ULg are greatly acknowledged for providing computational resources.

## Supporting Information Available

- SRO-TE-ESI: (1) Calculated structural properties of ground state  $\text{SrRuO}_3$  in comparison with other literature. (2) The calculated density of states of  $\text{SrRuO}_3$  with and without  $R_4^+$  mode.

This material is available free of charge via the Internet at <http://pubs.acs.org/>.

---

## References

- (1) Koster, G.; Klein, L.; Siemons, W.; Rijnders, G.; Dodge, J. S.; Eom, C.-B.; Blank, D. H.; Beasley, M. R. Structure, Physical Properties, and Applications of SrRuO<sub>3</sub> Thin Films. *Rev. Mod. Phys.* **2012**, *84*, 253.
- (2) Cuffini, S.; Guevara, J.; Mascarenhas, Y. Structural Analysis of Polycrystalline CaRuO<sub>3</sub> and SrRuO<sub>3</sub> Ceramics from Room Temperature up to 1273 K. *Mater. Sci. Forum.* 1996; pp 789–794.
- (3) Kennedy, B. J.; Hunter, B. A.; Hester, J. R. Synchrotron X-Ray Diffraction Reexamination of the Sequence of High-Temperature Phases in SrRuO<sub>3</sub>. *Phys. Rev. B* **2002**, *65*, 224103.
- (4) Junquera, J.; Ghosez, P. Critical Thickness for Ferroelectricity in Perovskite Ultrathin Films. *Nature* **2003**, *422*, 506–509.
- (5) Stengel, M.; Spaldin, N. A. Origin of the Dielectric Dead Layer in Nanoscale Capacitors. *Nature* **2006**, *443*, 679–682.
- (6) Ahn, C.; Hammond, R.; Geballe, T.; Beasley, M.; Triscone, J.; Decroux, M.; Fischer, O.; Antognazza, L.; Char, K. Ferroelectric Field Effect in Ultrathin SrRuO<sub>3</sub> films. *Appl. Phys. Lett.* **1997**, *70*.
- (7) Mackenzie, A.; Reiner, J.; Tyler, A.; Galvin, L.; Julian, S.; Beasley, M.; Geballe, T.; Kapitulnik, A. Observation of Quantum Oscillations in the Electrical Resistivity of SrRuO<sub>3</sub>. *Phys. Rev. B* **1998**, *58*, R13318.
- (8) Maekawa, T.; Kurosaki, K.; Muta, H.; Uno, M.; Yamanaka, S. Thermoelectric Properties of Perovskite Type Strontium Ruthenium Oxide. *J. Alloys Compd.* **2005**, *387*, 56–59.

- 
- (9) Klein, Y.; Hébert, S.; Maignan, A.; Kolesnik, S.; Maxwell, T.; Dabrowski, B. Insensitivity of the Band Structure of Substituted SrRuO<sub>3</sub> as Probed by Seebeck Coefficient Measurements. *Phys. Rev. B* **2006**, *73*, 052412.
- (10) Keawprak, N.; Tu, R.; Goto, T. Thermoelectric Properties of Sr-Ru-O Compounds Prepared by Spark Plasma Sintering. *Mater. Trans.* **2008**, *49*, 600–604.
- (11) Keawprak, N.; Tu, R.; Goto, T. Thermoelectric Properties of Alkaline Earth Ruthenates Prepared by SPS. *Mater. Sci. Eng. B* **2009**, *161*, 71–75.
- (12) Hébert, S.; Daou, R.; Maignan, A. Thermopower in the Quadruple Perovskite Ruthenates. *Phys. Rev. B* **2015**, *91*, 045106.
- (13) Keawprak, N.; Tu, R.; Goto, T. Thermoelectric Properties of Ca<sub>1-x</sub>Sr<sub>x</sub>RuO<sub>3</sub> Compounds Prepared by Spark Plasma Sintering. *J. Alloys Compd.* **2012**, *523*, 182–187.
- (14) Garcia-Fernandez, P.; Verissimo-Alves, M.; Bilc, D. I.; Ghosez, P.; Junquera, J. First-Principles Modeling of the Thermoelectric Properties of SrTiO<sub>3</sub>/SrRuO<sub>3</sub> Superlattices. *Phys. Rev. B* **2012**, *86*, 085305.
- (15) Puggioni, D.; Rondinelli, J. Designing a Robustly Metallic Noncentrosymmetric Ruthenate Oxide with Large Thermopower Anisotropy. *Nature Commun.* **2014**, *5*, 3432.
- (16) Singh, D. J. Electronic and Magnetic Properties of the 4d Itinerant Ferromagnet SrRuO<sub>3</sub>. *J. Appl. Phys.* **1996**, *79*, 4818–4820.
- (17) Allen, P.; Berger, H.; Chauvet, O.; Forro, L.; Jarlborg, T.; Junod, A.; Revaz, B.; Santi, G. Transport Properties, Thermodynamic Properties, and Electronic Structure of SrRuO<sub>3</sub>. *Phys. Rev. B* **1996**, *53*, 4393.
- (18) Shepard, M.; McCall, S.; Cao, G.; Crow, J. Thermodynamic Properties of Perovskite ARuO<sub>3</sub> (A=Ca, Sr, and Ba) Single Crystals. *J. Appl. Phys.* **1997**, *81*, 4978–4980.

- 
- (19) Zayak, A.; Huang, X.; Neaton, J.; Rabe, K. M. Structural, Electronic, and Magnetic Properties of SrRuO<sub>3</sub> Under Epitaxial Strain. *Phys. Rev. B* **2006**, *74*, 094104.
- (20) Rondinelli, J. M.; Caffrey, N. M.; Sanvito, S.; Spaldin, N. A. Electronic Properties of Bulk and Thin Film SrRuO<sub>3</sub>: Search for the Metal-Insulator Transition. *Phys. Rev. B* **2008**, *78*, 155107.
- (21) Miao, N.; Bristowe, N. C.; Xu, B.; Verstraete, M. J.; Ghosez, P. First-Principles Study of the Lattice Dynamical Properties of Strontium Ruthenate. *J. Phys.: Condens. Matter* **2014**, *26*, 035401.
- (22) Blochl, P. E. Projector Augmented-Wave Method. *Phys. Rev. B* **1994**, *50*, 17953.
- (23) Hafner, J. Ab-Initio Simulations of Materials Using VASP: Density-Functional Theory and Beyond. *J. Comput. Chem.* **2008**, *29*, 2044–2078.
- (24) Etz, C.; Maznichenko, I.; Böttcher, D.; Henk, J.; Yaresko, A.; Hergert, W.; Mazin, I.; Mertig, I.; Ernst, A. Indications of Weak Electronic Correlations in SrRuO<sub>3</sub> from First-Principles Calculations. *Phys. Rev. B* **2012**, *86*, 064441.
- (25) Grebinskij, S.; Masys, Š.; Mickevičius, S.; Lisauskas, V.; Jonauskas, V. Ab Initio and Photoemission Study of Correlation Effects in SrRuO<sub>3</sub> Thin Films. *Phys. Rev. B* **2013**, *87*, 035106.
- (26) Perdew, J. P.; Zunger, A. Self-Interaction Correction to Density-Functional Approximations for Many-Electron Systems. *Phys. Rev. B* **1981**, *23*, 5048.
- (27) Perdew, J. P.; Burke, K.; Ernzerhof, M. Generalized Gradient Approximation Made Simple. *Phys. Rev. Lett.* **1996**, *77*, 3865.
- (28) Perdew, J. P.; Ruzsinszky, A.; Csonka, G. I.; Vydrov, O. A.; Scuseria, G. E.; Constantin, L. A.; Zhou, X.; Burke, K. Restoring the Density-Gradient Expansion for Exchange in Solids and Surfaces. *Phys. Rev. Lett.* **2008**, *100*, 136406.

- 
- (29) Dovesi, R.; Orlando, R.; Civalleri, B.; Roetti, C.; Saunders, V. R.; Zicovich-Wilson, C. M. CRYSTAL: A Computational Tool for the Ab Initio Study of the Electronic Properties of Crystals. *Z. Kristallogr.* **2005**, *220*, 571–573.
- (30) Bilc, D.; Orlando, R.; Shaltaf, R.; Rignanese, G.-M.; Íñiguez, J.; Ghosez, P. Hybrid Exchange-Correlation Functional for Accurate Prediction of the Electronic and Structural Properties of Ferroelectric Oxides. *Phys. Rev. B* **2008**, *77*, 165107.
- (31) Madsen, G. K.; Singh, D. J. BoltzTraP. A Code for Calculating Band-Structure Dependent Quantities. *Comput. Phys. Commun.* **2006**, *175*, 67–71.
- (32) Jones, C.; Battle, P.; Lightfoot, P.; Harrison, W. The Structure of SrRuO<sub>3</sub> by Time-of-Flight Neutron Powder Diffraction. *Acta Crystallogr., Sect. C: Cryst. Struct. Commun.* **1989**, *45*, 365–367.
- (33) Orobengoa, D.; Capillas, C.; Aroyo, M. I.; Perez-Mato, J. M. AMPLIMODES: Symmetry-Mode Analysis on the Bilbao Crystallographic Server. *J. Appl. Crystallogr.* **2009**, *42*, 820–833.
- (34) Perez-Mato, J.; Orobengoa, D.; Aroyo, M. Mode Crystallography of Distorted Structures. *Acta Crystallogr., Sect. A: Found. Crystallogr.* **2010**, *66*, 558–590.
- (35) Glazer, A. The Classification of Tilted Octahedra in Perovskites. *Acta Crystallogr., Sect. B: Struct. Crystallogr. Cryst. Chem.* **1972**, *28*, 3384–3392.
- (36) Carpenter, M. A.; Howard, C. J. Symmetry Rules and Strain/Order-Parameter Relationships for Coupling Between Octahedral Tilting and Cooperative Jahn-Teller Transitions in ABX<sub>3</sub> Perovskites. I. Theory. *Acta Crystallogr., Sect. B: Struct. Sci* **2009**, *65*, 134–146.
- (37) Varignon, J.; Bristowe, N. C.; Bousquet, E.; Ghosez, P. Coupling and Electrical Control of Structural, Orbital and Magnetic Orders in Perovskites. *Sci. Rep.* **2015**, *5*, 15364.

- 
- (38) Lee, S.; Zhang, J.; Torii, S.; Choi, S.; Cho, D.-Y.; Kamiyama, T.; Yu, J.; McEwen, K.; Park, J.-G. Large In-Plane Deformation of RuO<sub>6</sub> Octahedron and Ferromagnetism of Bulk SrRuO<sub>3</sub>. *J. Phys.: Condens. Matter* **2013**, *25*, 465601.
- (39) Chiritescu, C.; Cahill, D. G.; Nguyen, N.; Johnson, D.; Bodapati, A.; Koblinski, P.; Zschack, P. Ultralow Thermal Conductivity in Disordered, Layered WSe<sub>2</sub> Crystals. *Science* **2007**, *315*, 351–353.

# Graphical TOC Entry

